Int. J. Electrochem. Sci., 14 **(2019)** 8393 – 8404, doi: 10.20964/2019.09.36

International Journal of
ELECTROCHEMICAL
SCIENCE
www.electrochemsci.org

Study on Charge Storage Mechanism of $NiCo_2O_4$ Nanoarray Grown on Ni Foam

Jing Di[1,*], *Huajun Zheng*[2], *Ropafadzo Jamakanga*[1], *Xikun Gai*[1], *Ruiqin Yang*[1]

[1] Zhejiang Provincial Key Lab for Chemical and Biological Processing Technology of Farm Product, School of Biological and Chemical Engineering, Zhejiang University of Science and Technology, Hangzhou 310023, P.R. China
[2] Department of Applied Chemistry, Zhejiang University of Technology, Hangzhou 310014, P.R. China
[*]E-mail: dijing@zust.edu.cn

Received: 1 May 2019 / *Accepted:* 29 June 2019 / *Published:* 31 July 2019

$NiCo_2O_4$ is one of the most intensively studied electrode materials of pseudocapacitor. In this work, the charge storage mechanism of $NiCo_2O_4$ nanoarray and the impact of morphology structure are studied. The relationship between peak current of cyclic voltammetric and sweep rate is investigated and the results show both capacitive and diffusion-controlled processes are occurred. The capacitive charges and diffusion-controlled charges are calculated separately and the capacitive charge storage only contributes 28.4%～66.3% of the total stored charges at 5 mV s^{-1} for different morphology samples. Even at 100 mV s^{-1}, a general number of stored charges are controlled by diffusion process. The influence of structure and morphology on charge storage process are also explored which demonstrate the overlapped and complex structures would increase the diffusion resistance and enlarge the diffusion time during fast energy storage processes. These results indicate

Keywords: $NiCo_2O_4$; capacitive charge; diffusion-controlled charge; charge storage mechanism

1. INTRODUCTION

$NiCo_2O_4$ has attracted considerable attention over the recent years as a potential electrode material owing to its attractive performance in supercapacitors. By partially substituting Ni^{2+} for Co^{2+}, $NiCo_2O_4$ exhibits higher electronic conductivity and enhanced electrochemical activity by utilizing the redox behavior of both nickel and cobalt compared with Co_3O_4 [1, 2]. Moreover, $NiCo_2O_4$ is a potential material with high safety, low cost, great abundance, and a high theoretical capacity [3, 4]. Due to these prominent features, $NiCo_2O_4$ has been extensively investigated to assess its potential applications in high performance energy storage devices. Although tremendous studies have been conducted, most of them are concentrating on improving the electrochemical performance either by fabricating different microstructures or increasing the electronic conductivity [5-14].

Nevertheless, there has been disagreement concerning that $NiCo_2O_4$ behaves more like a battery-type electrode material than a pseudocapacitor electrode material. Most of the publications however declare that it is a pseudocapacitive material [15-17]. The electrochemical features of nickel-cobalt oxide are not typical pseudocapacitive. In a cyclic voltammetry curve of $NiCo_2O_4$, narrow and sharp peaks are presented and the voltage separation between anodic and cathodic peaks is often large even at low scan rates [15, 16]. In a galvanostatic curve, plateaus are formed during the charge and discharge voltage profile with a large voltage hysteresis [18, 19]. According to the conception of pseudocapacitance raised by Conway [20], the behavior described above is a battery-type process which is controlled by diffusion in the bulks [16, 21]. Therefore, the intrinsic storage behavior of $NiCo_2O_4$ needs to be further dug. Unfortunately, few explorations have been devoted to this problem. Uncertainty still remains as to the storage mechanism of $NiCo_2O_4$.

In this paper, we try to reveal the charge storage behavior of $NiCo_2O_4$. The kinetics of capacitive and diffusion contributions were analyzed by studying the "current-sweep rate" power law relationship [22]. The charges stored by surface/near-surface and bulk diffusion were calculated separately. To eliminate the impact of the binder and conduct carbon, $NiCo_2O_4$ was grown directly on a Ni-foam current conductor and used as the electrode directly. Our study agrees with the opinion of Wang [15] that $NiCo_2O_4$ is a hybrid supercapacitor which both capacitive and diffusion-controlled capacity contribute to the whole energy storage. Further studies also illustrate how the microstructures influence the surface/near surface and bulk charge storage significantly.

2. EXPERIMENTAL

2.1 Synthesis of $NiCo_2O_4$ nanowires on Ni foam

All the regents were of analytical grade and were used without further purification. One mmol $Ni(NO_3)_2$•$6H_2O$ and 2 mmol $Co(NO_3)_2$•$6H_2O$ were dissolved in 80 mL deionized water to form a clear pink solution, then 12 mmol urea was added and the solution was stirred at 60 ºC for 30 min. The solution was then transferred into a 100 mL Teflon-lined stainless autoclave and Ni foam (1*4 cm) was placed in the solution. After heated at 120 ºC for different time in an oven, the autoclave was placed in the oven to cool down spontaneously. Then Ni foam was taken out, washed with deionized water and ethanol several times, following by cleaning with ultrasonication to remove loose powder attached on Ni foam. The hydrothermal times are 2 h, 6 h and 10 h, respectively and the corresponding samples are denoted as NCO-2, NCO-6 and NCO-10. After totally dried at 60 ºC, the Ni foam with as-prepared precursor was finally sintered at 400 ºC for 2 h under air atmosphere.

2.2 Material characterization

The crystal phase of $NiCo_2O_4$ powder scratched from Ni foam was examined by a X'Pert Pro diffractometer with a CuKα radiation source. The morphology of the samples was observed by scanning electron microscopy (SEM, Hitachi S-4800). The nitrogen adsorption was used to measure the surface area of samples by Micromeritics ASAP 2020 instrument.

2.3 Electrochemical measurements

The electrochemical performances including cyclic voltammogram (CV) and electrochemical impedance spectroscopy (EIS) were conducted by an IviumStat Vertex electrochemical workstation at room temperature with a three-electrode cell containing 2 M KOH aqueous solution where the as-prepared Ni foam as the working electrode, Pt foil as the counter electrode and a standard calomel electrode (SCE) as the reference electrode. The area of the working electrode immersed into the electrolyte was controlled to be 1 cm * 1 cm. EIS was recorded in the frequency ranges from 100 kHz to 10 mHz at open circuit potential with an AC amplitude of 5 mV.

3. RESULTS AND DISCUSSION

$NiCo_2O_4$ nanoarrays were synthesized using a hydrothermal method followed by sintering treatment. The hydrothermal times are 2 h, 6 h and 10 h, respectively, and the corresponding samples are denoted as NCO-2, NCO-6 and NCO-10. The samples are then analyzed to characterize the structure and morphology. Fig.1 shows the XRD patterns of NCO-2, NCO-6 and NCO-10 powder scratched from nickel foams. All the materials exhibit similar diffraction peaks at the same 2 θ values which can be assigned to $NiCo_2O_4$ phase (JCPDS card no.: 73-1702). No other impurity peaks are detected, confirming the formation of pure $NiCo_2O_4$ after hydrothermal process and sintering treatment.

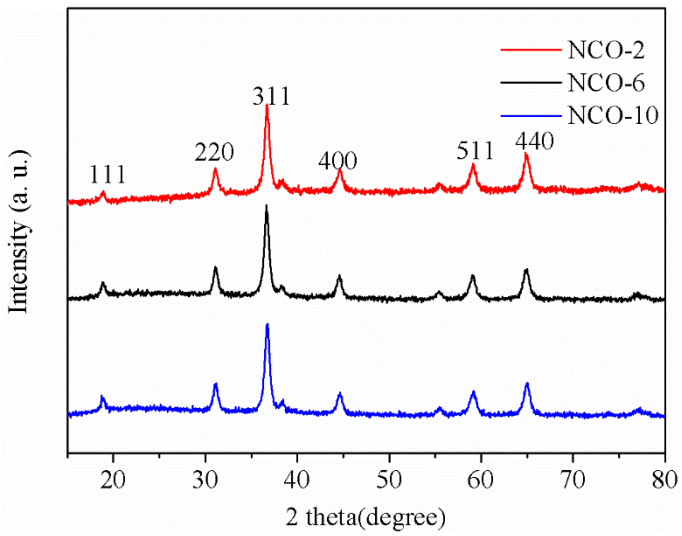

Figure 1. XRD patterns of NCO-2, NCO-6 and NCO-10.

The morphologies and structures of NCO-6 and NCO-10 were firstly examined by SEM. Fig. 2 a, b, d and e depict the top views while Fig. 2 c and f reveal the side view. For NCO-6, the surface of nickel foam is covered by vertically oriented and uniformly distributed nanowires with lengths of 1-2 μm and diameters of 50-100 nm. This morphology can be typically observed for metal oxide

nanoarrays grown on substrates [5, 6, 13]. Meanwhile, the images for NCO-10 are obviously different. As one can see, a large number of incompact urchin-like nanostructures, shown in insert image in Fig. 2 e, overlay on top of the uniformly and densely grown nanowires. More interestingly, the side views of both NCO-6 and NCO-10 in Fig. 2 c and f essentially illustrate that the observed nanowires actually grew on the top of the thick walls which look like formation of nanoplates.

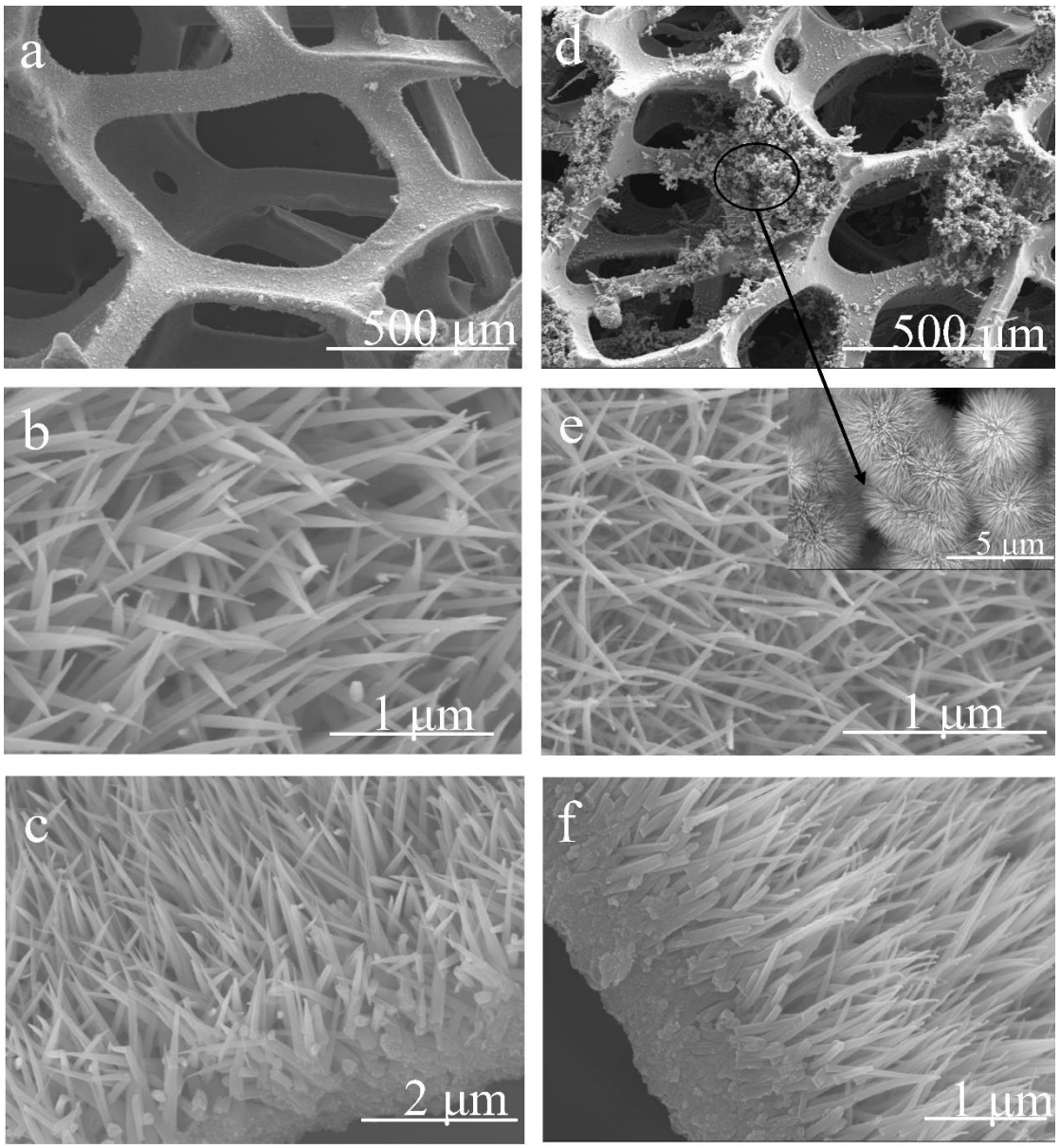

Figure 2. SEM images of NCO-6 (a, b and c) and NCO-10 (d, e and f).

To gain a better understanding of how this "urchin-on-nanowire-on-nanoplate-structure" formed, the SEM images of the $NiCo_2O_4$ arrays grown for 1.5 h, 2 h, 2.5 h and 3 h are examined and shown in Fig. 3. The results show that after hydrothermal treatment for 1.5 h, ultrathin plates form on the surface of nickel foam while some nano nuclei begin to form on the surface of nanoplates. (Fig. 3 a).

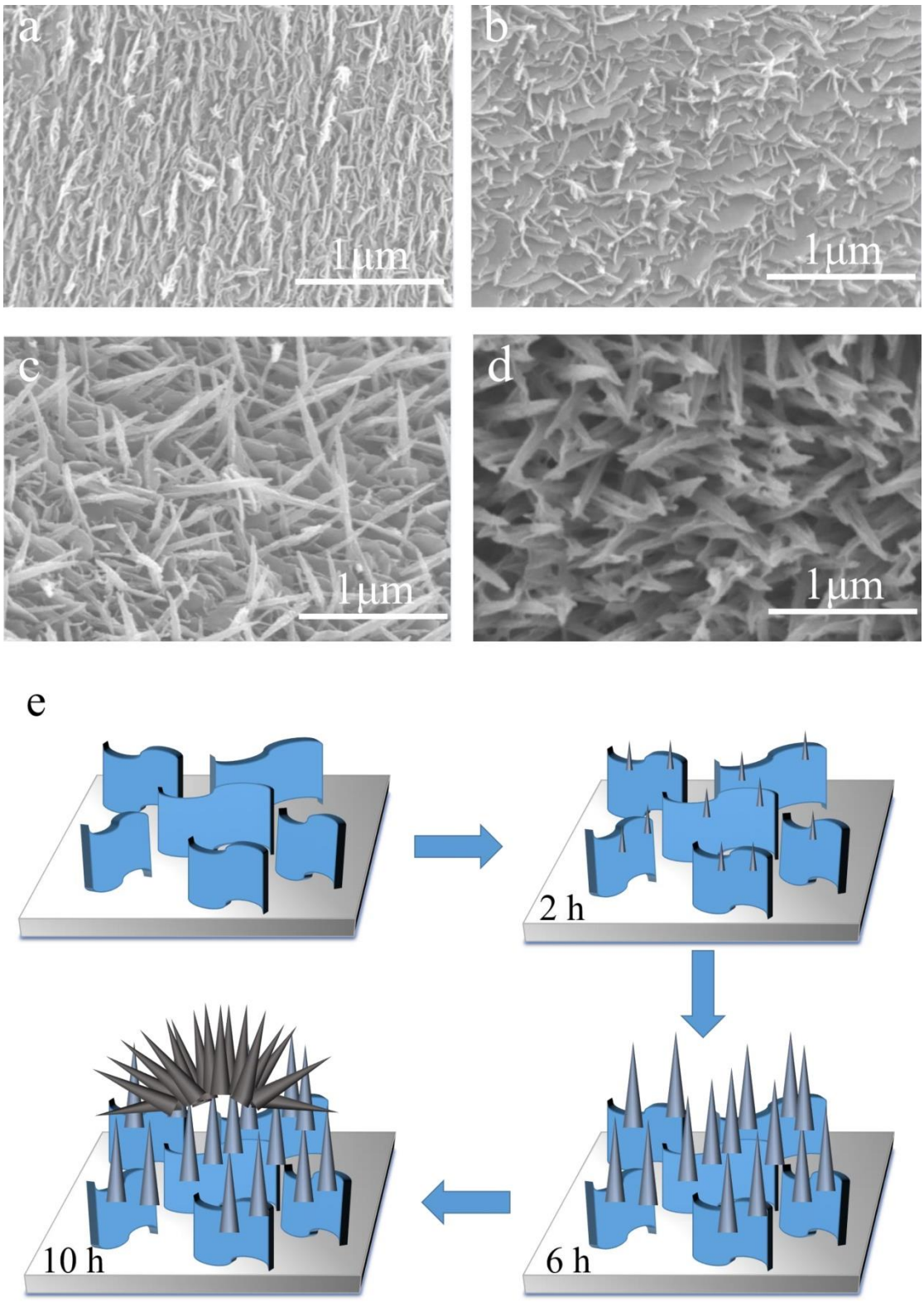

Figure 3. SEM images of $NiCo_2O_4$ grown on Ni foam for different time: a: 1.5 h, b: 2 h, c: 2.5 h, d: 3 h, and e: growth routine.

After 2 h, the small plates grow larger and the nano nuclei develop into long nanowires (Fig. 3 b). As the reaction time was prolonged, the numbers of nanowires on top of nanoplates increased and

the sizes became larger (Fig. 3 c). As shown in Fig. 3 d, uniform nanowires became sparsely populated and vertically aligned when the time was increased to 3 h. Meanwhile, no nanoplates can be observed in the image as they may be covered by the nanowires on top of the nanoplates.

From the morphology and structure images, the growing routine in hydrothermal process can thus be inferred (Fig. 3 e). At the initial stage of putting the nickel foam into the hydrothermal reactor, small nuclei began to gather on the surface of nickel foam. As the hydrothermal time increased, the former nuclei grew to form nanoplates and new nuclei started forming on top of the nanoplates. When the reaction time as further prolonged, the formerly small nanoplates grew bigger and started connecting to each other, forming a firm wall, while the nuclei on top of the nanoplates grew into long nanowires. The nanowires got interconnected and took root in nanoplates firmly. When the growth time was ultimately prolonged, the ions remaining in the solution gathered and finally grew to urchin-like structures because of the approaching to the minimum of the surface energy [21, 22]. These structures grew and adhered well on the top of the finely grown nanowires with the help of urea [23, 24]. Finally, the different layers interconnected with each other and formed the complex transport network. The similar growth mechanism is also discovered by several groups while they developed the hierarchical porous metal oxide nanowire cluster derived from nanosheet arrays on Ni foam or carbon clothe [23-25]. This self-assembly and the formation of layer-on-layer structure may be explained by Ostwald ripening [83], crystal-face attraction, van der Waals forces and hydrogen bonds [26-29].

CV measurements were conducted in a three-electrode cell to evaluate the performance of $NiCo_2O_4$. Fig. 4 shows the cyclic voltammograms at different scan rates in a potential range of 0-0.6 V. A pair of anodic and cathodic peaks with similar shapes shown at all the sweep rates corrsepond to the oxidation and reduction processes, indicating reversible Faradaic redox reactions occurred on the electrodes. The redox reactions of $NiCo_2O_4$ in alkaline electrolyte are as follows:

$$NiCo_2O_4 + OH^- + H_2O \leftrightarrow NiOOH + 2CoOOH + e^- \quad (1)$$

$$CoOOH + OH^- \leftrightarrow CoO_2 + H_2O + e^- \quad (2)$$

In equation (1), the electrochemical behavior is more like battery, and the energy storage process is limited by diffusion which would result in poor rate capability[30]. For equation (2), the redox reactions take place on the surface or near-surface which gives pseudocapacitance. According to this, the electrochemical performance of $NiCo_2O_4$ is the combination contribution of pseudocapacitance and battery capacity. However, $NiCo_2O_4$ is usually regarded as a pseudocapacitive material which storage behavior is controlled by surface reaction.

Further analysis based on CV results can help us to estimate the contribution of reaction on surface or bulk. As shown in Fig. 4, the shapes of the CV curves remain unchanged, while the peak currents increase with the increased scan rates. As the current responsed to a sweep rate in cyclic voltammetry curves is important to determine whether the redox reaction process is surface controlled or diffusion controlled [30, 31], the relationship between current and sweep rate was studied. At a specific voltage, current can be described by the following equation [31-33]:

$$i = av^b \quad (3)$$

where a and b are adjustable values. When the value of b is equal to 0.5, the current is controlled by an ideal semi-infinite diffusion process. When the value of b approaches to 1, it indicates that the current is surface-controlled; in other words, the process is capacitive. Furthermore, we can

deduce that the closer the b-value gets to 0.5, the more significant part of semi-infinite solid-state diffusion takes in the energy storage process.

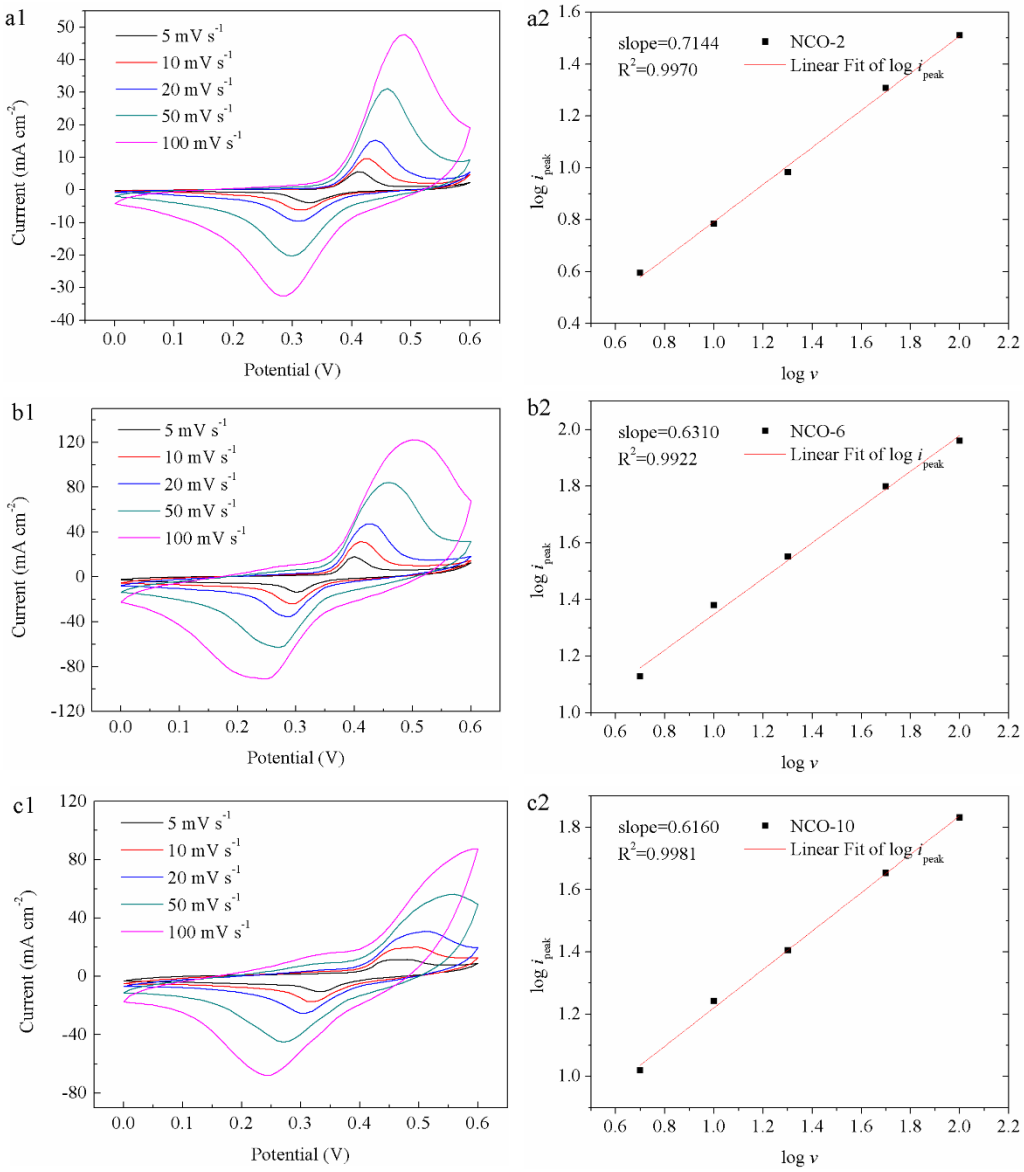

Figure 4. Cyclic voltammograms of NCO-2 (a1), NCO-6 (b1) and NCO-10 (c1) at various sweep rates and variation of peak current as a function of sweep rate of NCO-2 (a2), NCO-6 (b2) and NCO-10 (c2).

On the basis of this, we plotted log $i_{\text{cathodic peak}}$ versus log v in figure 3 and b-value was calculated from the slope of the plots. It can be seen that the linear fitting for all the samples is very good (R^2>0.99). The b-value of NCO-2, NCO-6 and NCO-10 is 0.7144, 0.6310 and 0.6160, respectively, which is intermediate between 0.5 and 1, implying the storage behavior is controlled by both surface reaction and diffusion processes. It can be seen that the b-value decreases in an order of

NCO-2>NCO-6>NCO-10. From the results we obtained, one can conclude that the limit of diffusion arises with increasing the hydrothermal growth time. This result indicates a good agreement between the capacity retention rates at different scan rates for NCO-2, NCO-6 and NCO-10. The capacity retention rate at 10 mV/s, 20 mV/s, 50 mV/s and 100 mV/s compared with 5 mV/s are 94%, 85%, 64%, and 45% for NCO-2, 90%, 72%, 48%, and 37% for NCO-6, and 70%, 42%, 24%, and 16% for NCO-10, respectively. That is to say, at the same large scan rate, the capacity retention shows the same order as NCO-2>NCO-6>NCO-10. As the hydrothermal growth time of the precursor increases, the hierarchical structure like NCO-6 and NCO-10 with high roughness may produce air pockets and prevent the electrolyte from reaching to the interface area between electrode and electrolyte, resulting in hydrophobicity of surface [34, 35]. Thus, this overlapped and hierarchical structure is not beneficial for electrolyte penetration. On the opposite, it can hinder the movement of electrolyte ions to achieve the active sites and thereby decrease the electrochemical performance especially the high rate properties.

To further explore the contribution of capacitive and diffusion-controlled processes, the capacities due to the two processes were separated based on the method suggested by Trasatti [36, 37]. According to Trasatti, the total energy Q_t stored by metal oxides is related to the *inner* and *outer* surfaces. The inner surface, which means the micro pores or channels inside of the nano particles, are less accessible and the capacity that occurs is due to diffusion process. The outer surface, corresponding to the surface on the particles or larger pores, is more reachable hence the relative capacity is surface capacitive. The total charge thus can be written as:

$$Q_t = Q_i + Q_o \quad (4)$$

where Q_i and Q_o are the charges related to the inner and outer surface, respectively. Then the relationship between the capacity and the sweep rate is stated as follows:

$$Q = Q_o + const(\frac{1}{\sqrt{v}}) \quad (5)$$

$$1/Q = (\frac{1}{Q_t} + const'(\sqrt{v}) \quad (6)$$

The dependence of Q on $v^{-1/2}$ and the inverse of Q on $v^{1/2}$ was draw, and the linearity is good (not shown). The extrapolation of Q to v=∞ from Q vs $v^{-1/2}$ plot gives the outer charge Q_o, and the extrapolation of Q^{-1} vs $v^{1/2}$ plot gives the total charge Q_t. The corresponding voltammetric charges are displayed in table 1.

Table 1. The charges density estimated and real charges density at 5 and 100 mV s^{-1} of different samples.

Sample	Q_t (C g^{-1})	Q_o (C g^{-1})	Q_i (C g^{-1})	Q_{r5}* (C g^{-1})	Q_{r100}** (C g^{-1})	Q_o / Q_t	Q_o / Q_{r5}	Q_o / Q_{r100}
NCO-2	1046.1	640.3	405.8	966.0	693.7	61.2%	66.3%	92.3%
NCO-6	909.1	310.3	598.8	736.5	396.6	34.1%	42.1%	78.2%
NCO-10	529.1	91.5	437.6	321.7	131.5	17.3%	28.4%	69.6%

*Q_{r5}: real Q at 5 mV s^{-1}; **Q_{r100}: real Q at 100 mV s^{-1}

The surface charge is 640.3 C/g for NCO-2 and this represents 61% in the total charge. The surface capacitive contributions for NCO-6 and NCO-10 decrease to 310.3 C/g and 91.5 C/g and the ratios to the overall charges also decrease to 34% and 17% respectively. It can be clearly seen that the capacitive contribution of $NiCo_2O_4$ grown over a shorter time is significantly larger than that of the samples grown over a longer period of time. The real charges at 5 mV s^{-1} and 100 mV s^{-1} and the ratios of Q_o to Q_r are also listed in Table 1. Similarly, the capacitive portions of both Q_{r5} and Q_{r100} decrease in the order of NCO-2>NCO-6>NCO-10.

Table 2. Comparison of the specific capacity of pseudocapacitive metal oxide materials at similar charge/discharge time

Materials	Specific capacity(C/g)	Charge/Discharge time(s)	References
$NiCo_2O_4$	105.6	120	26
$NiCo_2S_4$	~1265	~100	38
$Ni(OH)_2$-rGO	610	~120	39
Ni/Mn layered double hydroxides	571.4	~100	40
NiO/Ni-Co-Mn oxide	941.3	~100	41
$CuCo_2S_4$	1421.5	140	42
NCO-2	1046.1	120	This work

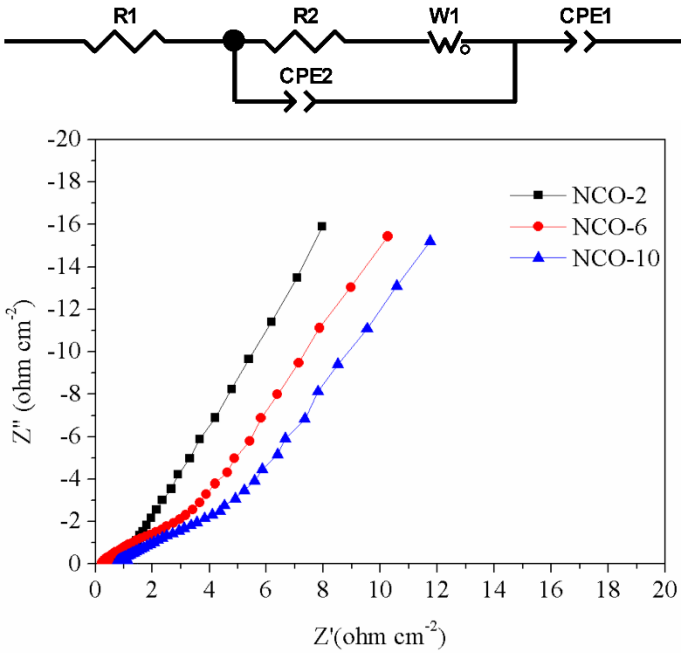

Figure 5. Nyquist plots at open circuit potential and the corresponding equivalent circuit.

Moreover, the contribution of diffusion is more pronounced at a low sweep rate than that at a

high sweep rate. The results presented here illustrate that the structure of NCO-2 insures that the outer surface is straightforwardly reachable, leading to the highest outer surface capacity among all the samples. The increase of diffusion contribution is stemmed from the complex structure and morphology, which prevents the movement of the electrolyte ions towards the electrode during charge/discharge process. Due to the faster kinetics associated with surface reaction, electrodes with a large fraction of Q_o in the total capacity are able to exhibit good rate properties.

We further compare the performance of LCO with other materials in the literatures and the results are demonstrated in Table 2. As it is shown, the specific charges and rate performance of our material can be comparable with the other electrode materials.

The electrochemical impedance spectroscopy (EIS) is a powerful technique to determine the electrochemical behavior. The Nyquist plots of all the samples were obtained at open circuit potential in the frequency range of 0.1-10^5 Hz with the corresponding equivalent circuit shown in the inset figure, as presented in Fig. 5. All the plots illustrate similar shapes, composed of a distorted semicircle at high and intermediated frequencies and a straight line at lower frequencies. In the equivalent circuit, R_s is the ohmic resistance of the test system, consisting of the intrinsic resistance of the active material and the substrate, the resistance of the electrolyte, and the contact resistance between the active material and substrate. R_{ct}, the charge-transfer resistance, which can also be calculated from the diameter of the semi-circle, can provide the information of dynamic property of redox reaction between the electrode and electrolyte. CPE_1 and CPE_2 are the limit capacitance and the constant phase element of double layer capacitance, respectively. *W*, the Warburg diffusion element, characterizes the OH^- diffusion during electrochemical process. The impedance of *W* is defined as:

$$Z(f) = R_d \frac{coth\sqrt{2\pi f t_d i}}{\sqrt{2\pi f t_d i}} \quad (7)$$

Where *f* is the frequency, R_d is the diffusion resistance and t_d is the diffusion time.

Table 3. Fitting values of R_s, R_{ct}, R_d and t_d.

Sample	R_s (Ω cm^{-2})	R_{ct} (Ω cm^{-2})	R_d (Ω cm^{-2})	t_d (s)
NCO-2	0.5125	0.2336	0.4884	0.009720
NCO-6	0.6172	2.045	7.111	0.3330
NCO-10	0.6564	3.710	8.839	0.4683

The fitting parameters based on the equivalent circuit are listed in Table 3. The equivalent circuit model yields an order of NCO-10>NCO-6>NCO-2 for R_s, R_{ct}, R_d and t_d, illustrating difficulty of kinetic processes including electron transfer and ion diffusion for samples with longer hydrothermal time. These kinetic analyses are consistent with capacity retention rates, current-sweep rate relationship and outer surface charge storage ratio, exhibiting that the energy storage process is controlled by diffusion in a deeper depth when the structure of electrodes is more complicated and overlapped.

4. CONCLUSIONS

$NiCo_2O_4$ nanoarrays with different structures were synthesized by hydrothermal process via adjusting the hydrothermal time. As the growth time increased, the morphology of the nanoarray appeared more complicated and finally, a "urchin-on-nanowire-on-nanoplate-structure" formed. The charge storage mechanism was quantitatively analyzed by "current-sweep rate" power law relationship and capacitive charge calculation. The results show both surface/near-surface and diffusion-controlled processes make contribution to the overall charge storage. As the hydrothermal time increased, the ionic diffusion and charge transfer resistance increase thus the diffusion process dominates the charge storage process. This study provides the deep insight into the charge storage mechanism of metal oxides and can give us the strategy to improve the rate capability by designing nanostructured materials with reduced diffusion path and resistance.

ACKNOWLEDGEMENTS
This work was supported by the National Science Foundation of Zhejiang province (grant numbers LQ18B030002, and LY 17B060002), Startup Foundation of Zhejiang University of Science and Technology (grant numberF701103G17) and Cross Pre-research Project of Zhejiang University of Science and Technology (grant number 2015JC05Y).

References

1. H. Chen, J. Jiang, L. Zhang, T. Qi, D. Xia, H. Wan, *J. Power Sources*, 248 (2014) 28.
2. J. Wu, P. Guo, R. Mi, X. Liu, H. Zhang, H. Liu, J. Mei, L.W.M. Lau, L.M. Liu, *J. Mater. Chem. A*, 3 (2015) 15331.
3. L. Ma, X. Shen, Z. Ji, X. Cai, G. Zhu, K. Chen, *J. Colloid Interf. Sci.*, 440 (2015) 211.
4. D.P. Dubal, P. Gomez-Romero, B.R. Sankapal, R. Holze, *Nano Energy*, 11 (2015) 377.
5. S. Chen, G. Yang, Y. Jia, H. Zheng, *J. Mater. Chem. A*, 5 (2016) 1028.
6. Y. Yuan, W. Wang, J. Yang, H. Tang, Z. Ye, Y. Zeng, J. Lu, *Langmuir*, 33 (2017) 10446.
7. S. Alrubaye, R. Rajagopalan, S.X. Dou, Z. Cheng, *J. Mater. Chem. A*, 5 (2017) 18989.
8. L. Cao, G. Tang, J. Mei, H. Liu, *J. Power Sources*, 359 (2017) 262.
9. C. Guan, X. Liu, W. Ren, X. Li, C. Cheng, J. Wang, *Adv. Energy Mater.*, 7 (2017) 1602391.
10. L. Wang, X. Jiao, P. Liu, Y. Ouyang, X. Xia, W. Lei, Q. Hao, *Appl. Surf. Sci.*, 427 (2017) 174.
11. F. Cui, Y. Huang, L. Xu, Y. Zhao, J. Lian, J. Bao, H. Li, *Chem. Commun.*, 54 (2018) 4160.
12. H. Rong, Z. Jiang, X. Tian, Y. Qin, S. Cheng, F. Wang, Z.J. Jiang, *J. Colloid Interf. Sci.*, 511 (2018) 119.
13. X. Wang, Y. Fang, B. Shi, F. Huang, F. Rong, R. Que, *Chem. Eng. J.*, 344 (2018) 311.
14. J. Zhao, Z. Li, X. Yuan, Z. Yang, M. Zhang, A. Meng, Q. Li, *Adv. Energy Mater.*, (2018) 1702787.
15. Q. Zhou, X. Wang, L. Yang, Y. He, Y. Gao, J. Liu, *J. Electrochem. Soc.*, 161 (2014) A1922.
16. T. Brousse, D. Belanger, J.W. Long, *J. Electrochem. Soc.*, 162 (2015) A5185.
17. C. Wang, E. Zhou, W. He, X. Deng, J. Huang, M. Ding, X. Wei, X. Liu, X. Xu, *Nanomaterials*, 7 (2017) 41.
18. Y. Lei, J. Li, Y. Wang, L. Gu, Y. Chang, H. Yuan, D. Xiao, *ACS Appl. Mater. Inter.*, 6 (2014) 1773.
19. Y. Chen, B. Qu, L. Hu, Z. Xu, Q. Li, T. Wang, *Nanoscale*, 5 (2013) 9812.
20. B.E. Conway, in: Power Sources Symposium, 1990., *Proceedings of the International*, 1991, pp. 319.
21. L. Hu, B. Qu, C. Li, Y. Chen, L. Mei, D. Lei, L. Chen, Q. Li, T. Wang, *J. Mater. Chem. A*, 1 (2013)

5596.
22. Y. Wang, P. Liu, K. Zhu, J. Wang, J. Liu, *Nanoscale*, 9 (2017) 14979.
23. Y. Chen, B. Qu, L. Hu, Z. Xu, Q. Li, T. Wang, *Nanoscale*, 5 (2013) 9812.
24. S. Chen, J. Wu, R. Zhou, Y. Chen, Y. Song, L. Wang, *RSC Adv.*, 5 (2015) 104433.
25. L. Hu, T. Shi, S. Jiang, S. Xi, R. Chen, S. Liu, G. Liao, Z. Tang, *J. Mater. Chem. A*, 2 (2014) 3741.
26. L. Wang, G. Liu, W. Wu, D. Chen and G. Liang, *J. Mater. Chem. A*, 3 (2015) 19497.
27. H. Long, T. Shi, S. Jiang, S. Xi, R. Chen, S. Liu, G. Liao and Z. Tang, *J. Mater. Chem. A*, 2 (2014) 3741.
28. A. Pan, H. B. Wu, L. Yu and X. W. D. Lou, *Angew. Chem.*, 125 (2013) 2282.
29. P. Liu, K. Zhu, Y. Gao, Q. Wu, J. Liu, J. Qiu, Q. Gu and H. Zheng, *CrystEngComm*, 15 (2013) 2753.
30. V. Augustyn, P. Simon, B. Dunn, *Energ. Environ. Sci.*, 7 (2014) 1597.
31. R. Li, J. Liu, *Electrochim. Acta*, 120 (2014) 52.
32. J.B. Mitchell, W.C. Lo, A. Genc, J. Lebeau, V. Augustyn, *Chem. Mater.*, (2017) 3928.
33. H. Lindström, S. Södergren, A. Solbrand, H. Rensmo, J. Hjelm, A. Hagfeldt, S.-E. Lindquist, *J. Phys. Chem. B*, 101 (1997) 7710.
34. B. Bhushan, Y.C. Jung, K. Koch, *Philos. T. Math. Phy. Eng. Sci.*, 367 (2009) 1631.
35. H. Adhikari, D. Neupane, C.K. Ranaweera, J. Candler, R.K. Gupta, S. Sapkota, X. Shen, S.R. Mishra, *Electrochim. Acta*, 225 (2017) 514.
36. D. Baronetto, N. Krstajić, S. Trasatti, *Electrochim. Acta*, 39 (1994) 2359.
37. S. Ardizzone, G. Fregonara, S. Trasatti, *Electrochim. Acta*, 35 (1990) 263.
38. J. Wang, R. Zhou, D. Jin, K. Xie, B. Wei, *Energy Storage Mater.*, 2 (2016) 1.
39. B. T. Zhao, L. Zhang, Q. B. Zhang, D. C. Chen, Y. Cheng, X. Deng, Y. Chen, R. Murphy, X. H. Xiong, B. Song, C.P. Wong, M.S. Wang, M. L. Liu, *Adv. Energy Mater.* 8 (2018) 1702247.
40. T. Li, J. Wang, Y. Xu , Y. Cao, H. Lin T. Zhang. *ACS Appl. Energy Mater.*, 1 (2018) 2242.
41. Z. Qin, R. Xu, B. Yu, W. Wang, Y. Zhang, *Int. J. Electrochem. Sci.*, 14 (2019) 2999.
42. A. Bahaa, J. Balamurugan, N. H. Kim , L. H. Jooh. *J. Mater. Chem. A*, 7 (2019) 8620.